Online Sensorless Position Estimation for Switched Reluctance Motors Using One Current Sensor

Chun Gan, *Student Member, IEEE*, Jianhua Wu, Yihua Hu, *Senior Member, IEEE*, Shiyou Yang, Wenping Cao, *Senior Member, IEEE*, and James L. Kirtley, Jr., *Life Fellow, IEEE*

***Abstract*—This paper proposes an online sensorless position estimation technique for switched reluctance motors (SRMs) using just one current sensor. It is achieved by firstly decoupling the excitation current from the bus current. Two phase-shifted pulse width modulation (PWM) signals are injected into the relevant lower-transistors in the asymmetrical half-bridge converter for short intervals during each current fundamental cycle. Analog to digital (A/D) converters are triggered in the pause middles of the dual-pulse to separate the bus current for excitation current recognition. Next, the rotor position is estimated from the excitation current, by a current-rise-time method in the current-chopping-control (CCC) mode in low-speed operation and a current-gradient method in the voltage-pulse-control (VPC) mode in high-speed operation. The proposed scheme requires only a bus current sensor and a minor change to the converter circuit, without a need for individual phase current sensors or additional detection devices, achieving a more compact and cost-effective drive. The performance of the sensorless SRM drive is fully investigated. The simulation and experiments on a 750-W three-phase 12/8-pole SRM are carried out to verify the effectiveness of the proposed scheme.**

***Index Terms*—Bus-current-sensor, position estimation, pulse width modulation (PWM), sensorless control, switched reluctance motors (SRMs).**

NOMENCLATURE

i_{bus}	Bus current
i_a, i_b, i_c	Currents for phases A, B and C
i_a', i_b', i_c'	Decoupled excitation currents for phases A, B and C
t_{on}	Turn-on time
t_{off}	Turn-off time
t_{shift}	Phase-shift time
f	Switching frequency
D	Duty-ratio
t_{min}	Minimum measurement time
u_k	Phase voltage
i_k	Phase current
i_{ref}	Current reference
R_k	Phase winding resistance
L_k	Phase winding inductance
i_{min}	Minimum of the chopping current
i_{max}	Maximum of the chopping current
$\triangle i$	Current hysteresis band
$\triangle t_n$	Current rise time
N_r	Number of rotor poles
ω	Rotor angular speed
f_s	Sampling frequency
θ_0	Critical rotor position where the rotor and stator poles start to overlap
θ_{err}	Angular error metric
θ_{est}	estimated rotor position
θ_{ref}	Actual rotor position

Manuscript received July 3, 2015; revised November 22, 2015; accepted November 30, 2015. This work was supported in part by the Chinese National 863 program (2011AA11A101) and National Nature Science Foundation of China (51377139).

C. Gan, J. Wu (*corresponding author*), and S. Yang are with the College of Electrical Engineering, Zhejiang University, Hangzhou 310027, China (e-mail: ganchun.cumt@163.com; hzjhwu@163.com; shiyouyang@yahoo.com).

Y. Hu is with the Department of Electronic and Electrical Engineering, University of Strathclyde, Glasgow, U.K. (e-mail: Yihua.hu@strath.ac.uk)

W. Cao is with the School of Engineering and Applied Science, Aston University, Birmingham, B4 7ET, U.K., and also with the Department of Electrical Engineering and Computer Science, Massachusetts Institute of Technology, Cambridge, MA 02139 USA. (e-mail: w.p.cao@aston.ac.uk)

J. L. Kirtley is with the Department of Electrical Engineering and Computer Science, Massachusetts Institute of Technology, Cambridge, MA 02139 USA. (e-mail: kirtley@mit.edu)

I. INTRODUCTION

In recent years, permanent magnet synchronous motors (PMSMs) are widely used in industrial applications [1]-[4], but they rely on the use of rare-earth-based permanent magnets. Considering the high cost and limited supply of rare-earth materials, switched reluctance motors (SRMs) have been attracting much attention due to their inherent advantages, including robust structure, low cost, high efficiency, and fault-tolerant ability. SRMs have a simpler rotor structure without any windings and permanent magnets. Hence, they are a competitive candidate for high-speed, high-temperature and safety-critical applications, such as electric locomotive traction [5], home appliances [6], [7] and electrified vehicles [8]-[11].

However, accurate rotor position is essential to the basic operation of SRMs. Conventionally, mechanical position sensors such as optical encoders, resolvers or Hall-effect sensors are installed on the motor frame to provide the precise rotor position information for motor control [12], but they inevitably add the cost to the drive and reduce the reliability of the motor system, which limit their industrial applications. For this reason, sensorless control for SRM drives is highly

desired [13]. Many advanced position sensorless control technologies for SRM drives have been developed, including the initial position detection for motor starting and reliable position sensorless control for motor running. In existing sensorless control methods, the main approaches can be classified as current waveform based methods [14]-[17], high frequency pulse injection methods [18]-[21], flux linkage based methods [22], [23], state observer based methods [24], [25], inductance model based methods [26]-[29], intelligent algorithm based methods [30]-[34], mathematical transformation methods [35]-[37], and circuit model based methods [38]-[40].

In the first method, the SRM sensorless operation can be achieved by measuring the chopping current and its rise time [14] or both the rise and fall times [15]. In [16] and [17], the rotor position of the SRM in high-speed operation of a PWM-voltage controlled system is estimated by the change of the phase current gradient when a rotor pole and stator pole start to overlap. A high frequency pulse is usually injected into an idle phase to obtain the SRM inductance characteristics for sensorless control [18]-[21]. However, this method leads to phase current distortion and a negative torque in the phase commutation region, which affects the performance of the motor drive. In [22], the flux linkage is obtained from the real-time current and voltage and is then fed into an artificial neural network or an adaptive neuro-fuzzy inference system for comparison with the flux linkage-current-rotor position characteristics, so as to predict the rotor position during running conditions. For a smaller memory and simpler computation, an improved flux linkage comparison scheme is proposed in [23], based on estimating a particular rotor position at both low and high speeds. However, for this scheme to work, the magnetic characteristics of the motor must be obtained previously, an extensive memory is needed to store the look-up tables, and the process is complicated and time-consuming. To deal with the issue, a sliding-mode-observer technology is employed in [24], [25] for four-quadrant sensorless operation of SRMs, covering a wide speed range. Yet another SRM sensorless control strategy is implemented in [26], by developing an incremental phase inductance model. In [27], a sensorless startup method for SRM is presented based on the region division of the measured unsaturated inductance. The SRM rotor position is estimated accurately by the phase inductance vectors and improved phase inductance subregion method [28]. A linear exponential regression method is adopted in [29] for SRM position estimation, by using a type-V exponential function to estimate the phase inductances. It involves injecting voltage pulses to all three phases simultaneously and measuring the phase currents individually. To improve the angle estimation accuracy of SRMs, some intelligent techniques are used for rotor position estimation, including the neural network [30], [31] and fuzzy logic [32]-[34]. The comparison between an artificial neural network and adaptive neuro-fuzzy inference system based techniques for the SRM is given in [22]. A position estimation algorithm based on a recursive least-squares estimator [35] deduces both position and speed, which is suited for operation at very low speed. By extracting the amplitude of the first switching harmonic in terms of the phase voltage and current, the rotor position can be estimated for a PWM period through the Fourier series, without any external hardware circuit [36]. In [37], a series of initial position estimation methods are presented, based on phase inductance vector coordinate transformations. In [38], the estimated rotor position is obtained by using a resonant circuit model, and the measurement accuracy depends on the associated resonance frequency. The circuit is naturally derived from a configuration comprising the SRM phase inductances and the parasitic capacitances of converter transistors, power cables, and motor windings. The initial position of the SRM is estimated in [39] by using bootstrap circuits and analyzing the time when the charging current reaches its peak in the bootstrap circuit, without predefined inductance parameters. However, this scheme could be only used for once if the bootstrap capacitor is not discharged. A sensorless control scheme is designed for a hybrid single-phase SRM based on the back-electromotive force (EMF) by using differential operational amplifier measurement circuits [40]. Another approach is proposed in [41], by using a similar SRM configuration to detect the rotor position.

In this paper, a real-time current detection method is developed for online position estimation. The accurate rotor position calculated from the phase current requires accurate current detection. Conventionally, a current sensor should be used in each phase to detect the phase current. In order to reduce the current sensors, some advanced low-cost current sensor placement technologies are reported to obtain the useful information from the bus current for motor drives [42]-[47]. As to sensorless SRM drives, although the position sensors have been removed, the current sensors used in the system still increase the cost and volume, and degrade the running reliability of the motor drives. Hence, a more compact, low-cost and high-reliable sensorless SRM drive is needed.

A new bus-current-sensor (BCS) based position estimation technique for SRM drives is proposed in this paper, by detecting excitation currents from the bus current. Described here is a dual-pulse injection scheme under phase-shift modulation that is used to find the excitation current in the whole excitation region. The BCS position estimation scheme can be implemented by using the decoupled excitation current based on a developed current-rise-time strategy and an improved current-gradient method over a wide speed range. Compared to traditional methods, only a single bus current sensor is needed in the proposed system without any additional detection circuit, and there is no need to inject high frequency pulses to idle phases. Alternatively, the pulses are only injected into the lower-transistors in the converter for brief intervals during each current fundamental cycle to detect the excitation current, which would not generate any negative torque and cause the phase current distortions, and switching loss is reduced due to the use of only the lower-transistors. Accurate estimation of motor characteristics and bus voltage are not required. The proposed sensorless drive has excellent robustness to fast transients, presenting good dynamic stability. The simulation and experimental tests on a 750-W three-phase

12/8-pole SRM are carried out to confirm the effectiveness of the proposed methodology.

II. Proposed Sensorless Position Estimation Scheme From Decoupled Excitation Current

A. Operational Modes of the SRM Drive

A conventional 12/8-pole SRM drive is shown in Fig. 1. An asymmetrical half-bridge converter is commonly used in the system to dive the motor, due to its phase isolation and fault-tolerant characteristics. The converter is composed by six switching devices S_1~S_6, which are clamped by the bus voltage. Therefore, the switching device voltage stress is the input voltage. To reduce the switching loss and torque ripple, a soft-chopping mode that the upper-transistor chops and lower-transistor remains closed in every phase turn-on cycle is usually employed [48]. Fig. 2 presents the basic operational modes of the converter circuit for phase A. In the conducting mode, power transistors S_1 and S_2 are both turned on, and the current flows in phase A windings, as shown in Fig. 1(a). In the freewheeling mode, S_1 is turned off and S_2 remains on in a soft-chopping mode, and the current is in a lower zero-voltage-loop (ZVL) though transistor S_2 and diode D_2, as shown in Fig. 2(b). In the demagnetization mode, S_1 and S_2 are both turned off to feed the current back to the power supply through D_1 and D_2, as shown in Fig. 2(c). The three modes are operated in turn in each current fundamental cycle, while only the conducting mode and freewheeling mode are related to the current excitation region. The states of phase windings in relation to the switching actions are illustrated in Table I.

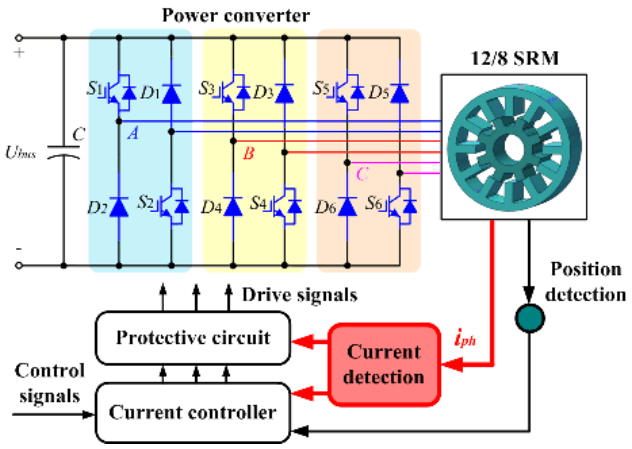

Fig. 1. 12/8-pole SRM drive.

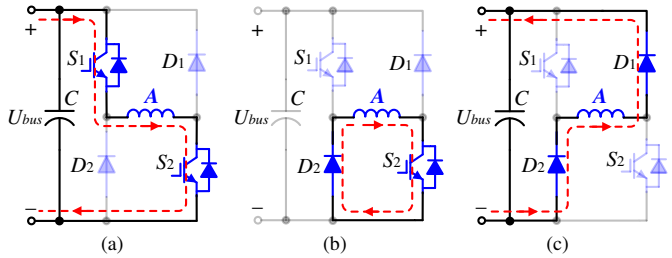

Fig. 2. Basic operational modes of the asymmetrical half-bridge converter. (a) Conducting mode. (b) Freewheeling mode. (c) Demagnetization mode.

TABLE I
Relationship of the Working Phases and Switching Actions

Working phase	Conducting device	State of phase
Phase A	S_1, S_2	Excitation
	D_2, S_2	Freewheeling
	D_1, D_2	Demagnetization
Phase B	S_3, S_4	Excitation
	D_4, S_4	Freewheeling
	D_3, D_4	Demagnetization
Phase C	S_5, S_6	Excitation
	D_6, S_6	Freewheeling
	D_5, D_6	Demagnetization

Fig. 3 shows the current control diagram for closed-loop SRM drives. The speed controller is used to regulate the motor speed and gives the current reference i^* for current regulation. The threshold logic calculates the maximum phase current, i.e., $i_{max}=i^*+\triangle i$, and the minimum phase current, i.e., $i_{min}=i^*-\triangle i$, to compare with the actual current for hysteresis control, where $\triangle i$ is the current hysteresis band. The rotor position is detected from a position sensor such as an encoder for phase commutation, and the motor speed is calculated from the rotor position for speed regulation.

The phase currents in the current-chopping-control (CCC) system at low speeds and voltage-pulse-control (VPC) system at high speeds are illustrated in Fig. 4. In CCC mode, when the phase current reaches i_{max}, the upper-transistor is turned off and the lower-transistor remains on, and the current will decrease in a ZVL, reducing it below i_{min}. Then, the upper-transistor is turned on to increase the phase current. When the phase current reaches its turn-off angle, the upper-transistor and lower-transistor are both turned off to recover stored magnetic energy. In high-speed operation, the chopping cycles contained in a phase conduction period are reduced greatly. In this condition, a VPC mode should be employed for motor control.

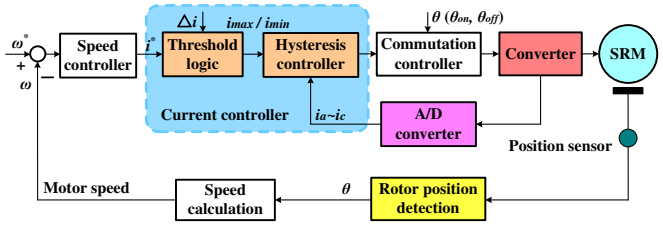

Fig. 3. Control diagram for closed-loop SRM drives with current hysteresis control.

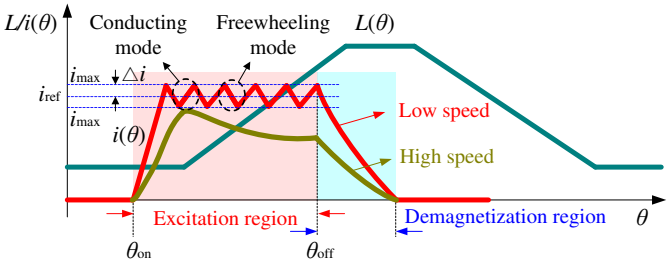

Fig. 4. Phase currents at low and high speeds.

B. Analysis of the Excitation Current

Phase currents and gate signals in CCC and VPC modes in low and high speed operation are shown in Figs. 5 and 6, respectively. In the figures, i_a, i_b, and i_c are the phase A, B and C currents, respectively; S_1, S_3, and S_5 are the gate signals for the upper-transistors of phases A, B and C, respectively; S_2, S_4, and S_6 are the gate signals for the lower-transistors of phases A, B and C, respectively; θ_1 and θ_3 are the turn-on angles for phases B and C; θ_2 and θ_4 are the turn-off angles for phases A and B; and θ_5 is the current depleting angle for phase B. Regions I and III are the excitation current overlapping regions; Regions II and IV are the excitation current non-overlapping regions.

The overlapped region in a current period between the two consecutive excitation currents can be expressed as

$$\Delta\theta = \theta_2 - \theta_1 = \theta_4 - \theta_3 \tag{1}$$

In Region I, the bus current is the sum of the excitation currents of phases A and B. In Region II, the excitation current of phase B and the demagnetization current of phase A are overlapped. However, if the demagnetization current of phase A is removed in this region, the bus current only contains the excitation current of phase B. Similarly, the bus current is the sum of the excitation currents of phases B and C in Region III. In Region IV, the excitation current of phase C and the demagnetization current of phase B are overlapped. However, if the demagnetization current of phase B is removed in Region IV, the bus current only contains the excitation current of phase C.

Therefore, if all the demagnetization currents are removed from Regions II and IV in Figs. 5 and 6, the bus current in the rotor position region of θ_1-θ_5 can be represented as

$$i_{bus} = \begin{cases} i_a + i_b, & \theta_1 < \theta \le \theta_2 \\ i_b, & \theta_2 < \theta \le \theta_3 \\ i_b + i_c, & \theta_3 < \theta \le \theta_4 \\ i_c, & \theta_4 < \theta \le \theta_5 \end{cases} \tag{2}$$

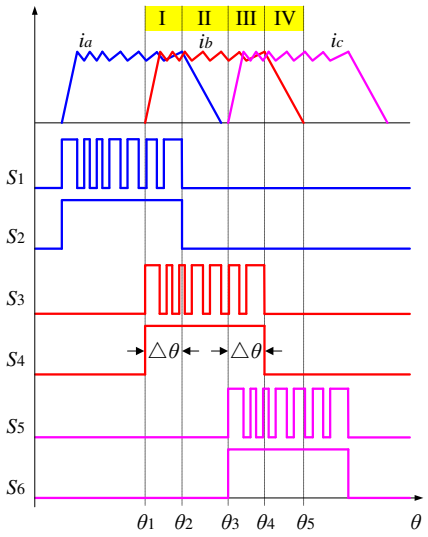

Fig. 5. Phase currents and gate signals under CCC in low-speed operation.

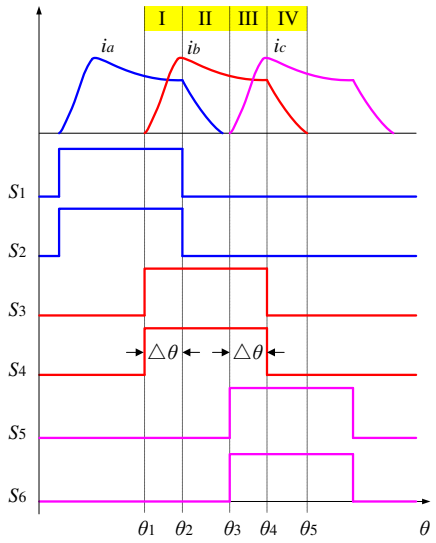

Fig. 6. Phase currents and gate signals under VPC in high-speed operation.

C. Proposed BCS Technique for Excitation Current Decoupling

Although the position sensors have been removed in the sensorless controlled SRM drives, individual current sensors installed in each phase leg still increase the cost and degrade the reliability of the sensorless drives. To achieve a more compact and reliable motor drive, a BCS placement strategy is developed, as presented in Fig. 7. The lower bus connection is separated into two parts. One is the connection of the anodes of all lower-diodes to the power supply, and another is the connection of the emitters of all the lower-transistors to the power supply. The current sensor is installed in the lower bus across the connection of the lower-transistors. The current flow in the new BCS drive is illustrated in Fig. 8. Clearly, only the phase current in the excitation region, i.e., excitation current, passes the current sensor, as shown in Fig. 8(a) and (b). The demagnetization current of each phase would not be present in the bus current due to this drive configuration in Fig. 8(c).

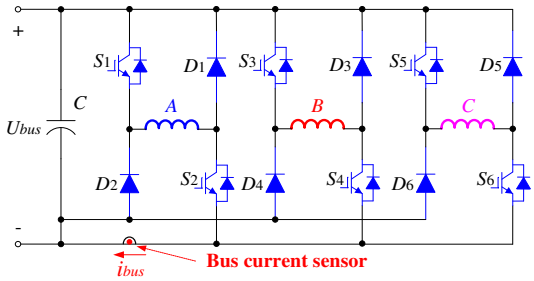

Fig. 7. BCS placement strategy.

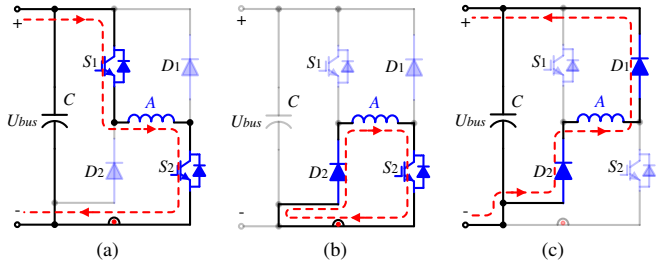

Fig. 8. Current flow in the new converter configuration. (a) S_1 on, S_2 on. (b) S_1 off, S_2 on. (c) S_1 off, S_2 off.

The switching functions for the lower-transistors in the converter are defined as

$$S_k = \begin{cases} 1, & \text{Lower-transistor is on} \\ 0, & \text{Lower-transistor is off} \end{cases}, \quad k = 2,4,6 \qquad (3)$$

Therefore, the bus current in the BCS drive can be expressed as

$$i_{bus} = i_a S_2 + i_b S_4 + i_c S_6 \qquad (4)$$

The bus current contained with the overlapped excitation currents under different switching states is illustrated in Table II (0: off, 1: on). Clearly, the excitation currents are overlapped when the related gate signals of the lower-transistors are overlapped, and six current states are determined according to the switching states.

TABLE II
BUS CURRENT UNDER DIFFERENT SWITCHING STATES

S_2	S_4	S_6	i_{bus}
1	0	0	i_a
1	1	0	i_a+i_b
0	1	0	i_b
0	1	1	i_b+i_c
0	0	1	i_c
1	0	1	i_a+i_c

In Region I, the bus current is the sum of the phase A and B currents. If the transistor S_2 is turned off, the phase A current will not flow in the bus current sensor, and the bus current only contains the phase B current. Similarly, if the transistor S_4 is turned off, the bus current only contains the phase A current. Hence, if the transistors S_2 and S_4 are turned off individually, the phase A and B currents can be obtained by

$$i_{bus} = \begin{cases} i_b, & S_2 = 0, S_4 = 1 \\ i_a, & S_2 = 1, S_4 = 0 \end{cases} \qquad (5)$$

In Region III, if the transistors S_4 and S_6 are turned off individually, the phase B and C currents can be obtained by

$$i_{bus} = \begin{cases} i_b, & S_4 = 1, S_6 = 0 \\ i_c, & S_4 = 0, S_6 = 1 \end{cases} \qquad (6)$$

Based on the analyses above, a dual-pulse injection technique is proposed for excitation current detection. A short low level of the pulse is injected into S_2 in Region I for excitation current of phase B detection and another phase-shifted pulse is injected into S_4 in Region I for excitation current of phase A detection.

It should noted that, in order to avoid two phases turning off in the same time when injecting the pulses, the phase-shift time t_{shift} should be limited and satisfy

$$t_{off} < t_{shift} < t_{on} \qquad (7)$$

In this paper, the phase-shift time is set as half of a pulse period. Fig. 9 shows the excitation current detection for phases A and B in their overlapped region in a current chopping period. Pulse1 is injected into the lower-transistor of phase B and an analog to digital (A/D) conversion channel, A/D1, is triggered in the pause middles of pulse1 to sample the bus current, which is directly the excitation current of phase A. Similarly, pulse2, with a half pulse period phase-shift time from pulse1, is injected simultaneously into the lower-transistor of phase A and another A/D conversion channel, A/D2, is triggered in the pause middles of pulse2 to sample the bus current, which is directly the excitation current of phase B. Hence, phase A and B currents can be easily decoupled from the bus current in the excitation current overlapping regions.

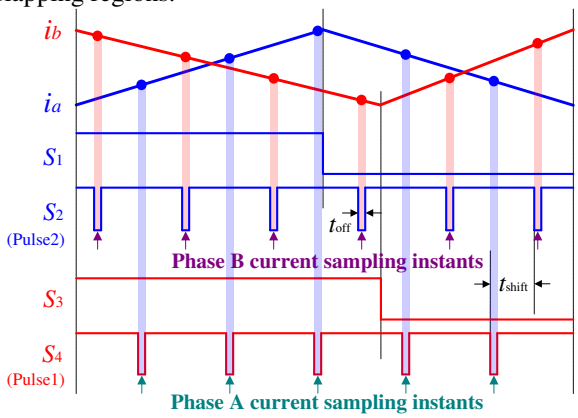

Fig. 9. Diagram of pulse1 and pulse2 injections into the lower-transistors of phases A and B in the current overlapping region for excitation current sampling and decoupling.

The diagram of the implemented pulse injection technique for all three phases is illustrated in Fig. 10. The excitation currents for phases A, B and C can be fully obtained by the following equations:

$$i_a' = i_{bus2} \cdot S_2 \cdot S_6 + i_{bus1} \cdot S_2 \cdot S_4 + i_{bus} \cdot S_2 \cdot \overline{S_2 S_6} \cdot \overline{S_2 S_4} \qquad (8)$$

$$i_b' = i_{bus2} \cdot S_2 \cdot S_4 + i_{bus1} \cdot S_4 \cdot S_6 + i_{bus} \cdot S_4 \cdot \overline{S_2 S_4} \cdot \overline{S_4 S_6} \qquad (9)$$

$$i_c' = i_{bus2} \cdot S_4 \cdot S_6 + i_{bus1} \cdot S_2 \cdot S_6 + i_{bus} \cdot S_6 \cdot \overline{S_4 S_6} \cdot \overline{S_2 S_6} \qquad (10)$$

where S_2, S_4 and S_6 are the gate signals prior to the pulse injection; i_a', i_b' and i_c' are the decoupled excitation currents for phases A, B and C; i_{bus1} and i_{bus2} are the sampled bus currents in pause middles of pulse1 and pulse2, respectively; and i_{bus} is the sampled bus current without any pulse injection.

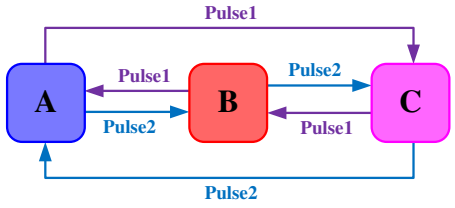

Fig. 10. Diagram of the implemented pulse injection scheme for all three phases.

The turn-off time t_{off} of the injected pulse should be extremely short, because it may lead to distortions in current and torque. In order to minimize the adverse impact and ensure a high sampling precision, the switching frequency and duty-ratio of the pulses should be set large enough for an extremely short turn-off time. On the other hand, the duty-ratio should be low enough for a sufficient acquisition time for current detection [49]. If the duty-ratio is much close to 1, the phase current may not be reliably detected because the

available acquisition times are too short. To ensure sufficient sampling time for current sensors and A/D converters, a minimum measurement time is determined by

$$t_{\min} = max(t_{cs}, t_{ad}) \tag{11}$$

where t_{cs} is the response time of the current sensor and t_{ad} is the acquisition time of the A/D converter.

Therefore, the switching frequency f and the duty-ratio D of the injected pulse should satisfy

$$t_{off} = \frac{1-D}{f} \geq t_{\min} \tag{12}$$

D. Position Estimation from Decoupled Excitation Current

The sensorless position estimation strategies, based on the current waveforms in the excitation regions, can be implemented directly by the decoupled excitation current that obtained from the bus current at low speeds or high speeds.

1) Low Speed Operation: When the motor operates at low speeds, the current rise time in a chopping period can be used to estimate the rotor position [14]. The adjacent current rise time in the excitation current is presented to make use of hysteresis current control in soft chopping mode, without the effects of winding resistance and bus voltage, as shown in Fig. 11.

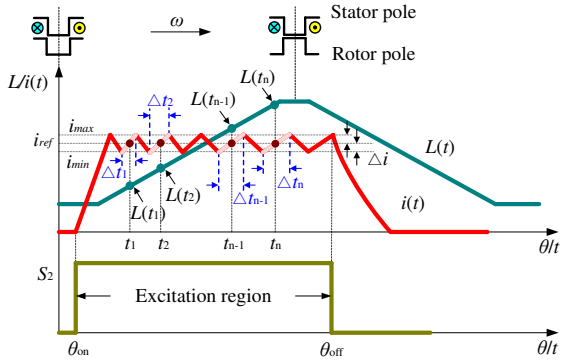

Fig. 11. Diagram of the developed current-rise-time method in low-speed operation.

In the excitation region, the applied phase voltage can be expressed as

$$u_k = R_k i_k(t) + L_k(t)\frac{di_k}{dt} + i_k(t)\frac{dL_k(t)}{dt} \tag{13}$$

where u_k is the phase voltage, R_k is the phase winding resistance, i_k is the phase current, L_k is the phase winding inductance, and k=a, b, c phase.

The applied phase voltages at t_{n-1} and t_n can be expressed as

$$\begin{cases} u_k(t_{n-1}) = R_k i_k(t_{n-1}) + L_k(t_{n-1})\dfrac{di_k(t_{n-1})}{dt} + i_k(t_{n-1})\dfrac{dL_k(t_{n-1})}{dt} \\ u_k(t_n) = R_k i_k(t_n) + L_k(t_n)\dfrac{di_k(t_n)}{dt} + i_k(t_n)\dfrac{dL_k(t_n)}{dt} \end{cases} \tag{14}$$

where t_{n-1} and t_n are the sampling instants for two consecutive chopping periods when the phase current reaches the current reference value i_{ref}.

Assuming that the inductance is linear in its non-saturated region, the phase inductance gradients at t_{n-1} and t_n yield

$$\frac{dL_k(t_{n-1})}{dt} = \frac{dL_k(t_n)}{dt} \tag{15}$$

The phase voltages and phase currents at t_{n-1} and t_n satisfy

$$\begin{cases} u_k(t_{n-1}) = u_k(t_n) = U_{bus} \\ i_k(t_{n-1}) = i_k(t_n) = I_{ref} \end{cases} \tag{16}$$

where U_{bus} is the bus voltage.

Therefore, according to (14), (15), and (16), the current gradients and phase inductances at t_{n-1} and t_n satisfy

$$L_k(t_{n-1})\frac{di_k(t_{n-1})}{dt} = L_k(t_n)\frac{di_k(t_n)}{dt} \tag{17}$$

The current gradients in a chopping period when the phase current is rising can be obtained by

$$\begin{cases} \dfrac{di_k(t_{n-1})}{dt} = \dfrac{i_{max} - i_{min}}{\Delta t_{n-1}} = \dfrac{(i_{ref} + \Delta i) - (i_{ref} - \Delta i)}{\Delta t_{n-1}} = \dfrac{2\Delta i}{\Delta t_{n-1}} \\ \dfrac{di_k(t_n)}{dt} = \dfrac{i_{max} - i_{min}}{\Delta t_n} = \dfrac{(i_{ref} + \Delta i) - (i_{ref} - \Delta i)}{\Delta t_n} = \dfrac{2\Delta i}{\Delta t_n} \end{cases} \tag{18}$$

where i_{max} and i_{min} are the maximum and minimum values of the chopping current, $\triangle t_{n-1}$ and $\triangle t_n$ are the current rise times for two consecutive chopping periods, and $\triangle i$ is the current hysteresis band.

Hence, (17) can be represented further as

$$\frac{L_k(t_n)}{L_k(t_{n-1})} = \frac{\Delta t_n}{\Delta t_{n-1}} \tag{19}$$

The relationship between the current rise time and inductance is shown in Table III. Clearly, the rotor position for $\triangle t_n < \triangle t_{n-1}$ can be set as the turn-off angle, which is easily detected by comparing the current rise times in two consecutive chopping periods.

TABLE III
RELATIONSHIP BETWEEN CURRENT RISE TIME AND INDUCTANCE

Current rise time	Inductance
$\triangle t_n > \triangle t_{n-1}$	$L_k(t_n) > L_k(t_{n-1})$
$\triangle t_n < \triangle t_{n-1}$	$L_k(t_n) < L_k(t_{n-1})$
$\triangle t_n = \triangle t_{n-1}$	$L_k(t_n) = L_k(t_{n-1})$

After the determination of the turn-off angle, the motor speed and other rotor positions can be estimated by

$$\begin{cases} \omega = \dfrac{\Delta\theta_t}{\Delta t} = \dfrac{360^\circ}{\Delta t \cdot N_r} \\ \theta(k+1) = \theta(k) + \dfrac{\omega}{f_s} \end{cases} \tag{20}$$

where N_r is the number of rotor poles; $\triangle\theta_t$ is the angle interval between the adjacent detected positions, which is equivalent to 45° in a three-phase 12/8-pole SRM; $\triangle t$ is the time interval between the two consecutive turn-off positions;

$\theta(k+1)$ and $\theta(k)$ are the estimated angles at the adjacent sampling points; and f_s is the sampling frequency.

2) High Speed Operation: When the motor operates at high speeds, the chopping cycles contained in a phase conduction period would reduce or even disappear, which limits the resolution of the relative rotor position estimates. A VPC scheme is employed for high-speed operations. The relationship between the phase current, phase inductance and rotor position in VPC mode at high speeds is shown in Fig. 12.

In this condition, the current-gradient method can be employed for the rotor position estimation from the excitation current [16]. A developed method by comparing the current gradient of the excitation current in the pulse control system is presented in Fig. 12. θ_0 is a critical rotor position where the rotor and stator poles start to overlap, and simultaneously, the phase current reaches its peak, which can be used to estimate the rotor position. θ_0^- and θ_0^+ are the rotor positions before and after θ_0.

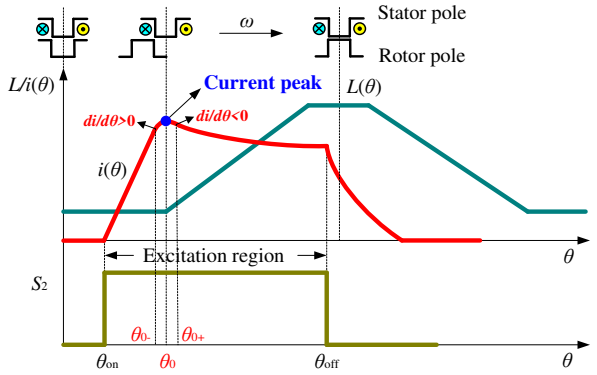

Fig. 12. Diagram of the developed current-gradient method in high-speed operation.

In the excitation region, the phase voltage equation can also be written as

$$u_k = R_k i_k(\theta) + L_k(\theta)\omega\frac{di_k}{d\theta} + i_k(\theta)\omega\frac{dL_k(\theta)}{d\theta} \tag{21}$$

where ω is the rotor angular speed, and θ is the rotor position.

The phase voltages at the rotor position θ_0^- and θ_0^+ are

$$\begin{cases} u_k(\theta_{0^-}) = R_k i_k(\theta_{0^-}) + L_k(\theta_{0^-})\omega\dfrac{di_k(\theta_{0^-})}{d\theta} + i_k(\theta_{0^-})\omega\dfrac{dL_k(\theta_{0^-})}{d\theta} \\ u_k(\theta_{0^+}) = R_k i_k(\theta_{0^+}) + L_k(\theta_{0^+})\omega\dfrac{di_k(\theta_{0^+})}{d\theta} + i_k(\theta_{0^+})\omega\dfrac{dL_k(\theta_{0^+})}{d\theta} \end{cases} \tag{22}$$

The phase inductance at θ_0^- satisfies

$$\frac{dL_k(\theta_{0^-})}{d\theta} = 0 \tag{23}$$

Thus, (22) can be represented further as

$$\begin{cases} u_k(\theta_{0^-}) = R_k i_k(\theta_{0^-}) + L_k(\theta_{0^-})\omega\dfrac{di_k(\theta_{0^-})}{d\theta} \\ u_k(\theta_{0^+}) = R_k i_k(\theta_{0^+}) + L_k(\theta_{0^+})\omega\dfrac{di_k(\theta_{0^+})}{d\theta} + i_k(\theta_{0^+})\omega\dfrac{dL_k(\theta_{0^+})}{d\theta} \end{cases} \tag{24}$$

The phase voltage, phase current and phase inductance will not change at θ_0^- and θ_0^+, which is given by

$$\begin{cases} u_k(\theta_{0^-}) = u_k(\theta_{0^+}) \\ i_k(\theta_{0^-}) = i_k(\theta_{0^+}) \\ L_k(\theta_{0^-}) = L_k(\theta_{0^+}) \end{cases} \tag{25}$$

Hence, according to (24) and (25), the relationship between the current gradients at θ_0^- and θ_0^+ can be expressed as

$$\frac{di_k(\theta_{0^-})}{d\theta} - \frac{di_k(\theta_{0^+})}{d\theta} = \frac{i_k(\theta_{0^+})}{L_k(\theta_{0^+})}\frac{dL_k(\theta_{0^+})}{d\theta} > 0 \tag{26}$$

θ_0 can be easily obtained by the current gradient variations, and the motor speed and other rotor positions can also be calculated from (20). In this operation condition, the turn-on angle should be set less than θ_0 to ensure the current peak appears at θ_0 for rotor position estimation.

However, it should be noted that, the initial rotor positions for phases A, B and C are required to determine the initial turn-on angular position of each phase for the implementation of the proposed BCS based position sensorless control strategy.

E. Comparison of the Existing and Proposed Schemes

A detailed comparison of the proposed position sensorless technique with existing methods is presented in Table IV. The current rise or fall time [14], [15] and current gradient [16], [17] are calculated based on the phase current waveform to estimate the rotor position. However, each phase should be equipped with a current sensor and the variations of the control parameters are not considered in these methods. High frequency pulse injection schemes are employed in [18]-[21], while these easily lead to phase current distortions and negative torques in the phase commutation region. In [22]-[25], the prior knowledge of flux linkage-current-rotor position characteristics is required as well as an extensive memory to store the look-up tables. This adds to the system complexity and operational time. Similarly, intelligent algorithm based methods [30]-[34] and mathematical transformation methods [35]-[37] are utilized for rotor position estimation, which are relatively complex and difficult. Additional detection devices including differential operational amplifier measurement circuits [40] and a similar SRM configuration [41] are utilized for position detection, which increase the cost and complexity to the motor drive.

Compared to the existing position sensorless schemes, the proposed scheme uses only one current sensor without any additional detection devices and much change to the circuitry, so as to considerably reduce the volume and complexity of the motor drive. The prior knowledge of motor magnetic characteristics is not required. The proposed scheme is found to be more accurate and easier to implement for position estimation, with lower current distortion from bus current detection. The added cost is determined by the number of current sensors and the additional detection devices employed in the motor drive. The proposed scheme offers a low-cost solution to SRM sensorless control. It has excellent robustness to the variations of system parameters including the speed, angle and load variations, which will be proved in the following sections.

TABLE IV
COMPARING OF EXISTING AND PROPOSED SCHEMES

	Paper [14]-[17]	Paper [18]-[21]	Paper [22]-[25]	Paper [30]-[37]	Paper [40], [41]	Proposed method
Current sensor	One for each phase	One for each phase	One for each phase	One for each phase	One for each phase	One for all phase
Motor magnetic characteristics	Not required	Required	Required	Not required	Not required	Not required
Circuitry change	No	No	No	No	No	Minor
Additional detection device	Not required	Not required	Not required	Not required	Required	Not required
Current distortion	Low	High	Medium	Low	Medium	Low
Implementation	Easy	Medium	Complicated	Complicated	Medium	Easy
Robustness	High	Medium	Low	High	Low	High
Cost	Medium	Medium	Medium	Medium	High	Low

III. SIMULATION RESULTS

A 750-W three-phase 12/8-pole prototype SRM is simulated in MATLAB/Simulink, as shown in Fig. 13(a). The current controller block is used to generate the conventional gate signals for power transistors, according to the given speed, turn-on angle and turn-off angle. The pulse injection block is used to generate the new gate signals for the lower-transistors to decouple the overlapped excitation currents. Pulse1 and pulse2 with the same frequency and duty-ratio under phase-shift modulation are injected simultaneously into the lower-transistors for the excitation current detection from the bus current. The converter is built with the components in the SimPowerSystems. The velocity is calculated from the load torque and phase torque that exports from the phase model. The theoretical rotor position is calculated from the angular velocity through the actual rotor position calculation block. The estimated rotor position is calculated from the decoupled excitation current and compared with the theoretical rotor position.

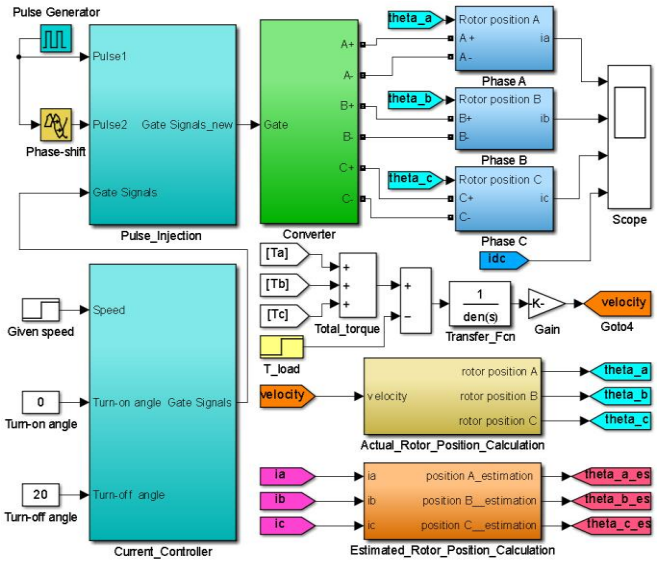

(a)

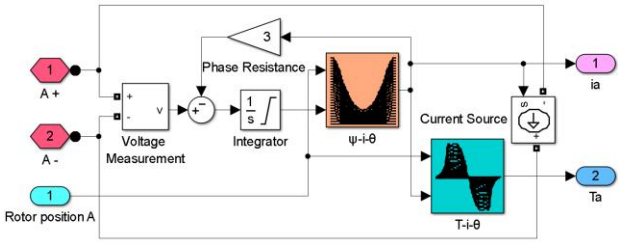

(b)

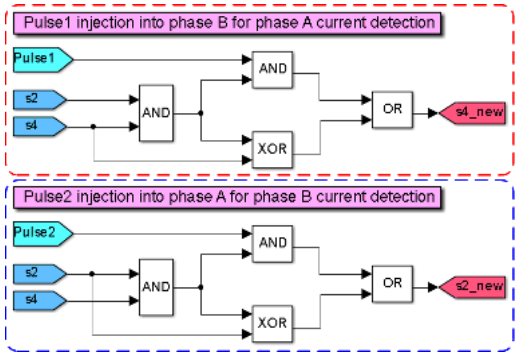

(c)

Fig. 13. Simulation model of the SRM drive. (a) System model. (b) SRM model for one phase. (c) Pulse injection module.

Fig. 13(b) shows the phase model of the SRM. Two look-up tables including the flux-current-position (ψ-i-θ) and torque-current-position (T-i-θ) characteristics obtained from numerical electromagnetic analysis by Ansoft software are used to build the SRM model. The phase current and phase torque are derived from the phase model. Fig. 13(c) shows the pulse injection module in the overlapped region between phases A and B. S_2 and S_4 are the gate signals in the lower-transistors of phases A and B prior to pulse injection, and S_{2_new} and S_{4_new} are the new gate signals for phases A and B after pulse injection. The frequency and duty-ratio of the injected pulse are set to 20 kHz and 95%, respectively, and the phase-shift time between pulse1 and pulse2 is set to 25 μs.

Fig. 14 shows the operational condition at 300 r/min in the CCC system. The turn-on and turn-off angles are set to 1.5° and 24°, respectively, and the current hysteresis band is set to 0.05 A. Clearly, the excitation currents are overlapped in the excitation regions, and the bus current is the sum of the three excitation currents, as shown in Fig. 14(a). For instance, in

order to decouple the overlapped excitation current of phases A and B in their overlapped region, pulse1 and pulse2 are injected into the lower-transistors of phases B and A respectively, as shown in Fig. 14(b). The bus current is resolved into two parts in the overlapped region, and the phase A and phase B current profiles are clearly obtained under the dual-pulse injection. Fig. 14(c) shows the excitation current decoupling state for phase B in the whole excitation region, and the lower envelope of the bus current is directly the excitation current of phase B.

The rotor position of phase B can be estimated from the decoupled excitation current by employing the developed current-rise-time method at low speed, as shown in Fig. 14(d). Although the second current rise time $\triangle t_2$ is shorter than the first current rise time $\triangle t_1$, they should not be used for rotor position estimation, because the excitation current rises from zero to i_{max} in the first chopping period while the current rises from i_{min} to i_{max} in the second chopping period. The last current rise time $\triangle t_n$ is shorter than $\triangle t_{n-1}$ when the excitation current reaches i_{max}, where the rotor position of phase B is 24°. At this position, phase B should be turned off immediately and the rotor position can be estimated accordingly. Obviously, the estimated rotor position obtained from the decoupled excitation current matches well with the theoretical rotor position.

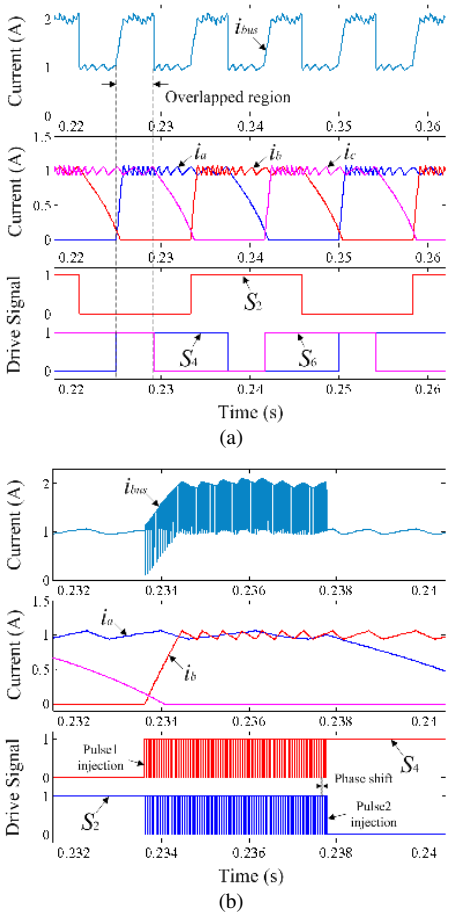

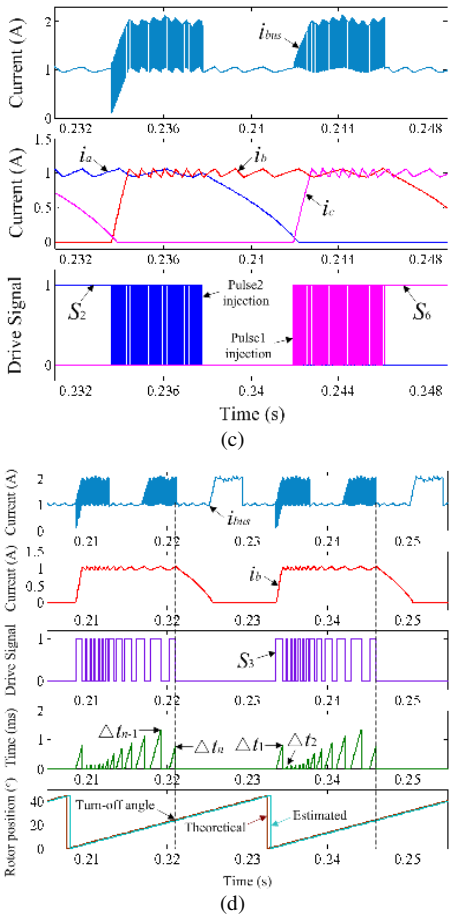

Fig. 14. Simulation results for low-speed operation. (a) Excitation current overlapping state. (b) Pulse1 and pulse2 injections for phase A and B currents detection in their overlapped region. (c) Excitation current decoupling for phase B in the whole excitation region. (d) Rotor position estimation from bus current based on current-rise-time method.

Fig. 15 shows the operation condition at 1500 r/min in the VPC system. The turn-on and turn-off angles are set to 0° and 20°, respectively. Fig. 15(a) shows the excitation current overlapping condition. The pulse injection method is implemented for phase A and B currents decoupling in their overlapped region, as shown in Fig. 15(b), and the excitation current detection for phase B in the whole excitation region is shown in Fig. 15(c). The implementation of the excitation current detection strategy in the VPC system is the same as that in the CCC system. Fig. 15(d) shows the rotor position estimation from the bus current based on the current-gradient method at high speed. An indicative position pulse is generated when the current gradient changes from positive to negative, where the phase current reaches its peak value. The critical position can be easily determined by the variations of the current gradient, and the estimated rotor position also shows a good agreement with the theoretical one.

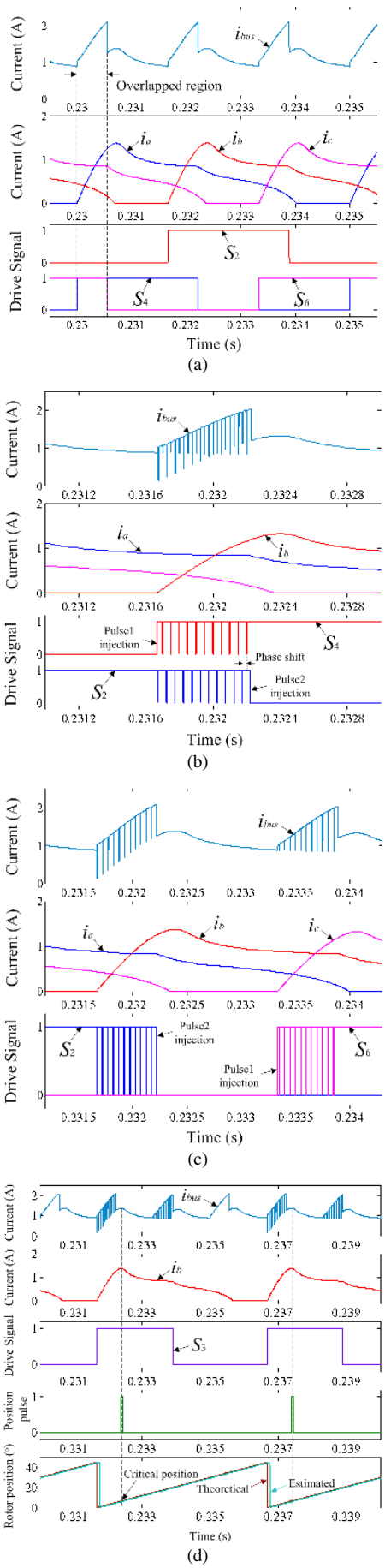

Fig. 15. Simulation results for high-speed operation. (a) Excitation current overlapping state. (b) Pulse1 and pulse2 injections for phase A and B currents detection in their overlapped region. (c) Excitation current decoupling for phase B in the whole excitation region. (d) Rotor position estimation from bus current based on current-gradient method.

IV. Experimental Verification

The proposed BCS sensorless technique is experimentally validated on a 750-W three-phase prototype SRM. The main motor system parameters are illustrated in Table V, and the photograph of the experimental setup is shown in Fig. 16. A dSPACE-DS1006 platform is employed as the main controller for implementing the proposed control algorithm. An asymmetrical half-bridge converter is employed in the system to drive the SRM. The power transistors are IGBT IKW75N60T and diodes are IDW75E60. A dc power supply with the output voltage of 60 V is utilized in the system. A magnetic brake is used as the load of the SRM. The bus current is measured by a Hall-effect current sensor (LA55P), and sampled by two 14-bit A/D conversion channels for the excitation current detection. For comparison, three additional current sensors are installed in three phase legs to measure the actual phase currents. A 2500-line incremental encoder is installed on the motor frame to measure the actual rotor position for comparing with the estimated one. The experimental waveforms are captured by a multi-channel oscilloscope.

TABLE V
Motor System Parameters

Parameters	Value
Phase number	3
Number of stator poles	12
Number of rotor poles	8
Rated speed (r/min)	1500
Rated power (W)	750
Phase resistor (Ω)	3
Minimum phase inductance (mH)	27.2
Maximum phase inductance (mH)	256.7
Rotor outer diameter (mm)	55
Rotor inner diameter (mm)	30
Stator outer diameter (mm)	102.5
Stator inner diameter (mm)	55.5
Stack length (mm)	80
Stator arc angle (deg)	14
Rotor arc angle (deg)	16
Encoder lines	2500
Switching devices (IGBT)	IKW75N60T
Diode	IDW75E60
Current sensors	LA55P

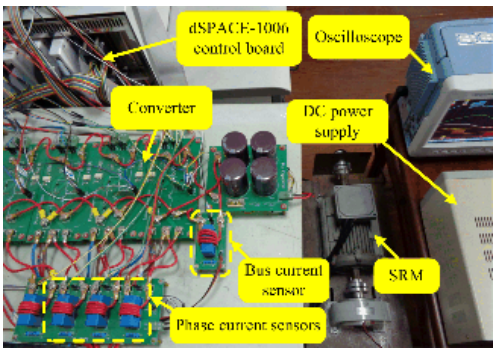

Fig. 16. Experimental setup.

Fig. 17 illustrates the schematic diagram of the implemented sensorless control strategy. As shown in the figure, two pulses with the same frequency and duty-ratio under phase-shift modulation are simultaneously injected into the lower-transistors of the related phase legs to generate the new switching signals for converter driving, and the A/D conversion channels are triggered in the pulse pause middles to sample the bus current through the operational amplifiers for excitation current detection. The estimated rotor position is obtained from the decoupled excitation current for speed calculation and phase commutation. A current-based controller with current hysteresis modulation is designed to regulate the phase current with a current hysteresis band of 0.05 A. A proportional and integral (PI) control algorithm is employed as the closed-loop controller to regulate the motor speed, and the proportional gain and integral gain are set to 0.05 and 0.5, respectively. The injected pulses are running with 20 kHz switching frequency, 95 % duty-ratio, and 25 μs phase-shift time, which are the same as those in the simulation.

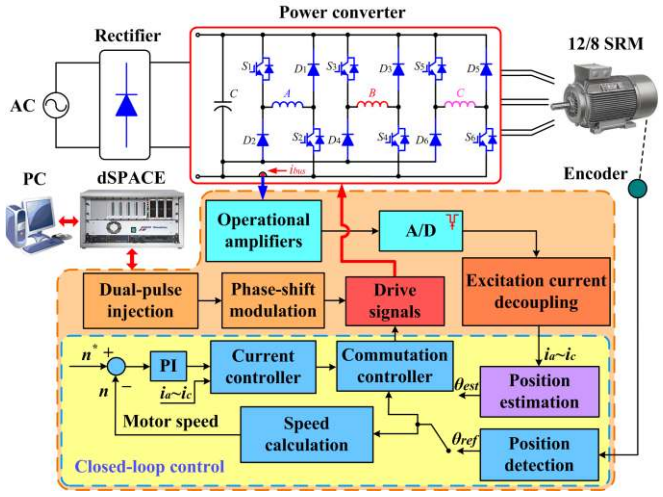

Fig. 17. Schematic diagram of the implemented position sensorless control strategy.

A. *Position Estimation under Excitation Current Decoupling*

Fig. 18 shows the experimental results of the excitation current decoupling at 300 r/min. The turn-on and turn-off angles are set to 1.5° and 24°, respectively. As shown in Fig. 18(a), the excitation currents are overlapped in the related regions in normal working states. The three phase currents have the same waveform with a 15° phase-shift, and the bus current is the sum of the three phase currents in their excitation regions. In order to decouple the overlapped excitation currents from the bus current, the proposed dual-pulse injection scheme is implemented in the overlapped regions, as shown in Fig. 18(b). Pulse1 is injected into the lower-transistor of phase B in the overlapped excitation region of phases A and B, and the lower-transistor of phase B is shut off during these inserted detection states. Phase B current is not contained in the bus current in the turn-off states of pulse1 and only phase A current is present in the bus current. Hence, the excitation current of phase A can be easily detected when A/D1 is triggered in the pause middle of pulse1. Similarly, pulse2, shifted by a half period from pulse1, is injected into the lower-transistor of phase A in the overlapped excitation region of phases A and B, and the lower-transistor of phase A is shut off during these inserted detection states. Phase A current is not contained in the bus current in the turn-off states of pulse2 and only phase B current is present in the bus current. If A/D2 is triggered in the pause middle of pulse2, the excitation current of phase B can be detected. Therefore, the bus current is separated into phase A and B currents easily in the overlapped regions. Fig. 18 (c) shows the excitation current decoupling for phase B in its whole excitation region. Pulse2 and pulse1 are simultaneously injected into the lower-transistors of phases A and C in their overlapped regions, respectively, and the whole excitation current of phase B can be obtained. Clearly, the bus current profile matches well with the phase B current, which also shows a good agreement with the simulation results. Fig. 18(d) shows a comparison of the decoupled excitation current from bus current and the actual sampled current using phase current sensor in the excitation region. Due to a large duty-ratio of the injected pulse, the turn-off time in a pulse period is extremely short, which has little impact on the actual phase current. The maximum current error is 0.02 A. Therefore, the decoupled excitation current successfully tracks the actual sampled current in the excitation region, confirming a good accuracy.

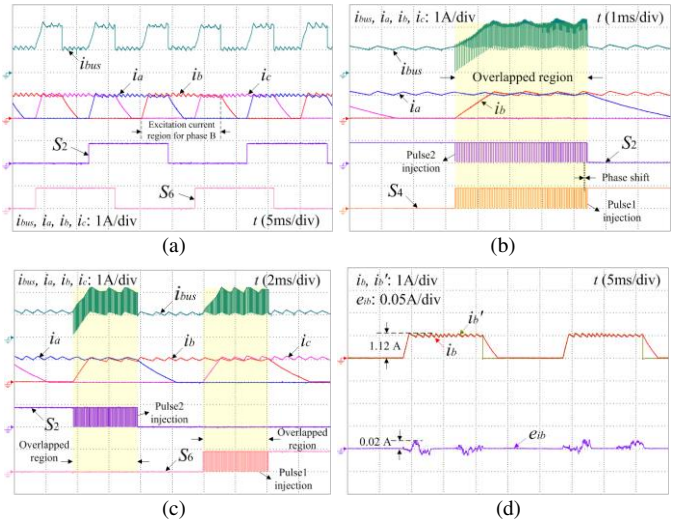

Fig. 18. Experimental results of excitation current decoupling in low-speed operation. (a) Excitation current overlapping state. (b) Pulse1 and pulse2 injections for phase A and B currents decoupling in their overlapped region. (c) Excitation current decoupling for phase B in the whole excitation region. (d) Excitation current comparison.

The current rise time in a chopping period can be further calculated based on the decoupled excitation current from the bus current, as shown in Fig. 19. The turn-on angles are set to 1.5° and -1.5° in Fig. 19(a) and (b), respectively. The current rise time variations are the same as that in the simulation. Although the first two chopping periods satisfy $\triangle t_2 < \triangle t_1$, they are not suited for rotor position estimation, because the excitation current rises from 0 to i_{max} in the fist chopping period whereas the excitation current rises from i_{min} to i_{max} in the second chopping period. Clearly, the rotor position where

$\triangle t_n < \triangle t_{n-1}$ is obtained. The turn-off angle can be easily determined by comparing two consecutive current rise times when the decoupled excitation current rises from i_{min} to i_{max} in spite of different turn-on angles, and other rotor positions can also be easily calculated based on the estimated turn-off angle.

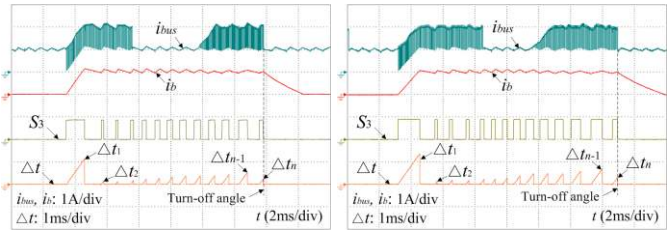

(a) (b)

Fig. 19. Current rise time calculation from decoupled excitation current. (a) Turn-on angle 1.5°. (b) Turn-on angle -1.5°.

To compare the estimated rotor position from the bus current and the actual one from the incremental encoder, an angular error metric, θ_{err}, is defined as

$$\theta_{err} = \theta_{est} - \theta_{ref} \tag{27}$$

where θ_{est} is the estimated rotor position and θ_{ref} is the actual rotor position.

For instance, the estimated rotor position of phase B is observed using a multichannel D/A converter with a low-pass filter, and compared with the actual rotor position in Fig. 20. The turn-on angle is set to 1.5° and -1.5° in Fig. 20(a) and (b), respectively. By injecting the pulses into the lower-transistors of phases A and C in the overlapped regions, the excitation current of phase B is separated from the bus current. The rotor position of phase B can be calculated based on the excitation current waveforms. From the experimental results, it can be seen that both the actual position and estimated position are rounded between 0° and 45° mechanical degrees for each current period. The estimated rotor positions under different turn-on angles match well with the actual ones, confirming the effectiveness of the proposed method for sensorless control.

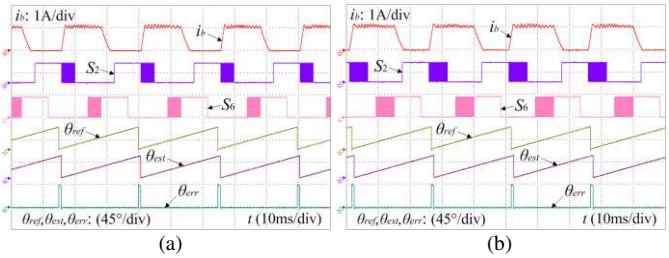

(a) (b)

Fig. 20. Rotor position estimation from decoupled excitation current based on current-rise-time method. (a) Turn-on angel 1.5°. (b) Turn-on angel -1.5°.

Fig. 21 shows the experimental results of the excitation current decoupling at 1500 r/min. The turn-on and turn-off angles are set to 0° and 20°, respectively. The excitation current can also be obtained from the bus current by employing the dual-pulse injection scheme, as shown in Fig. 21(b) and (c). Fig. 21(d) shows the current comparison between the decoupled excitation current and actual sampled one. The maximum current error is 0.022A in the excitation region, confirming a good accuracy in high-speed operation. The turn-on angle is set to 0° in Fig. 22(a) and -4° in Fig. 22(b). The critical position where the rotor and stator poles start to overlap is obtained by determining the current gradient when it changes from positive to negative, in spite of different turn-on angles, and an indicative position pulse is generated at the critical position. The other rotor positions can be fully calculated according to the location of the critical position. As shown in Fig. 23, the estimated position tracks the actual position well in high-speed operation, confirming the effectiveness of the proposed scheme over a wide speed range. Although the position estimation error exists in different operating modes, the estimated position is accurate enough for sensorless control of the machine.

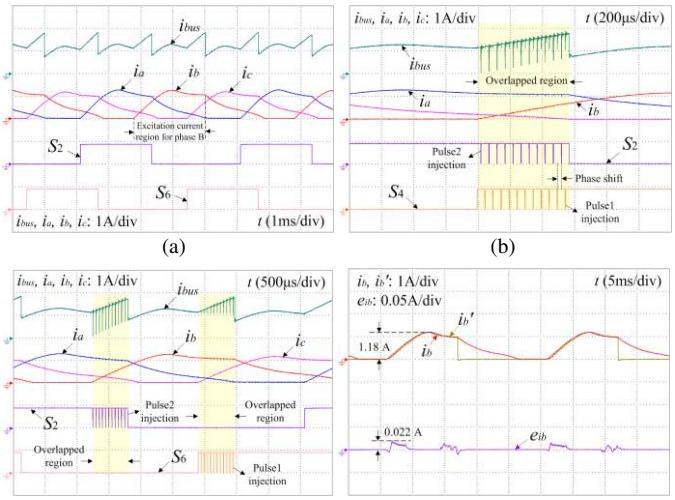

(a) (b)

(c) (d)

Fig. 21. Experimental results of excitation current decoupling in high-speed operation. (a) Excitation current overlapping state. (b) Pulse1 and pulse2 injections for phase A and B currents decoupling in their overlapped region. (c) Excitation current detection for phase B in the whole excitation region. (d) Excitation current comparison.

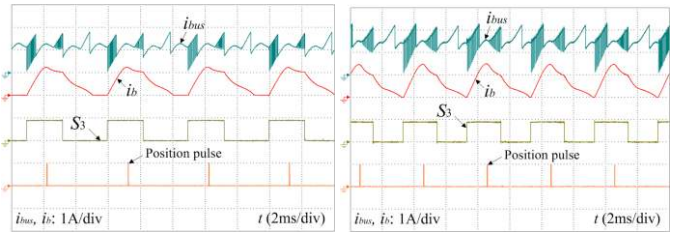

(a) (b)

Fig. 22. Position detection pulse generation based on current-gradient calculation from decoupled excitation current. (a) Turn-on angle 0°. (b) Turn-on angle -4°.

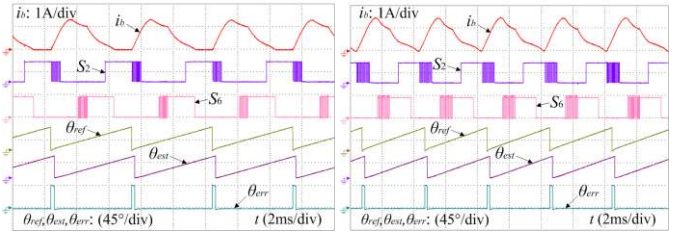

(a) (b)

Fig. 23. Rotor position estimation from decoupled excitation current based on current-gradient method. (a) Turn-on angel 0°. (b) Turn-on angel -4°.

B. Implementation of the BCS Sensorless Control Scheme in the Speed Controlled SRM Drive

The decoupled excitation current can be directly used for current regulation control, which implements the BCS sensorless control algorithm in CCC mode. When phase B is turned on, pulse1 is injected immediately into the lower-transistor of phase B to detect the excitation current of phase A for phase A position estimation and rotational speed calculation. Similarly, when phase C is turned on, pulse1 is immediately injected into the lower-transistor of phase C to detect the excitation current of phase B for phase B position estimation and rotational speed calculation; when phase A is turned on, pulse1 is immediately injected into the lower-transistor of phase A to detect the excitation current of phase C for phase C position estimation and rotational speed calculation. Hence, if the initial rotor position is known, the BCS position sensorless control can be implemented by employing the pulse injection technique for the three phases in turn.

Fig. 24 shows the transient response when the encoder signals are removed, where *Enc_A* and *Enc_B* are the pulse signals of the incremental encoder. In this case, the estimated rotor position is immediately put into to use instead of the actual rotor position. The system can smoothly transit to the sensorless operation, providing fault tolerant control for position signal faults. Fig. 25 shows the position estimation at startup and after an encoder fault. In Fig. 25(a), it can be seen that the rotor position can be accurately estimated from the excitation current in startup operations. In encoder fault conditions, the position signal from the encoder is lost and the rotor position can still be calculated according to the decoupled excitation current. The system can operate satisfactorily in a sensorless control state following an encoder fault without much transient fluctuation.

The transient response of the speed-controlled position sensorless system to fast transients is illustrated in Fig. 26. Fig. 26(a) shows the speed regulation conditions. The current reference is limited to 2 A in the acceleration progress to ensure the position detection from the chopping current. The motor speed is rapidly stabilized at the given value when it rises from 300 to 600 r/min and from 600 to 900 r/min. The actual speed follows the command speed well despite the speed changes during acceleration. Fig. 26(b) and (c) show the load variation conditions. When the load increases from 1 to 2 N·m and decreases from 2 to 1 N·m at low speed, the estimated speed both stabilizes within 200 ms, as shown in Fig. 26(b). In high-speed operations, the speed can still be easily controlled when the load changes suddenly, as shown in Fig. 26(c). Fig. 26(d) shows the angle modulation conditions when the turn-on angle suddenly changes from 1.5° to -1.5°. The speed is stabilized at the initial speed during this progress, presenting good dynamic stability. Therefore, the proposed position sensorless system has excellent robustness to fast transients including the speed regulation, load variation and angle modulation.

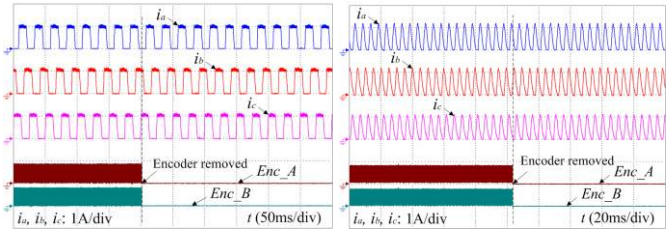

Fig. 24. Transient operation when the encoder signals are lost. (a) 300 r/min. (b) 1500 r/min.

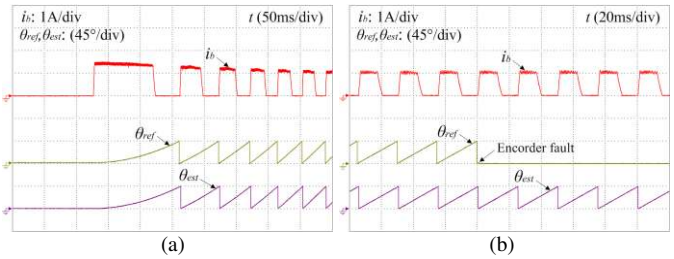

Fig. 25. Position estimation at startup and encoder fault. (a) Startup. (b) Encoder fault.

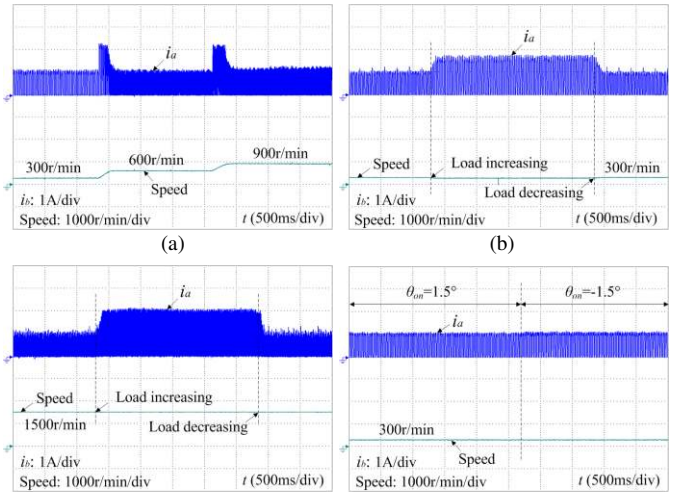

Fig. 26. Transient response to step changes. (a) Speed regulation. (b) Load variation at 300 r/min. (c) Load variation at 1500 r/min. (d) Angle modulation.

Fig. 27 presents an efficiency comparison between the proposed sensorless scheme and the traditional methods without sensorless control. For low-power SRMs, the system efficiency is relatively low [50]-[53]. However, it is still clear that the efficiency is not obviously degraded in the proposed system by using the proposed sensorless control scheme while the number of current sensors is reduced to one.

In order to study the effect of the proposed scheme on the SRM torque ripple, a further comparison is made between the proposed and traditional methods, as shown in Fig. 28. Clearly, the proposed method does not give rise to the torque ripple.

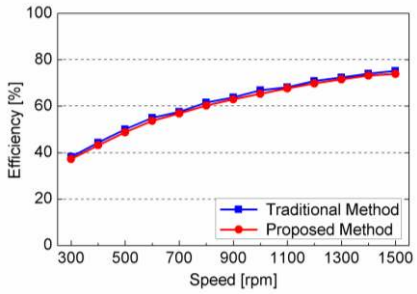

Fig. 27. Efficiency comparison.

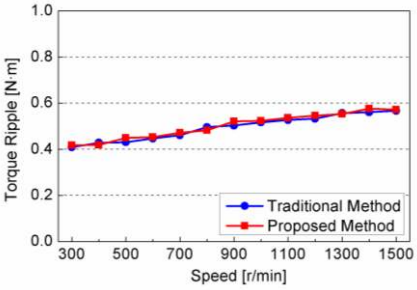

Fig. 28. Torque ripple comparison.

V. Conclusion

Although position sensors are absent in sensorless controlled SRM drives, current sensors in each phase still add to the cost and degrade the reliability of the system. To achieve a more reliable and cost-effective position sensorless drive, a new BCS based sensorless technique is proposed in this paper to reduce the number of current sensors used. A dual-pulse injection scheme is presented for excitation current decoupling from the bus current. Two phase-shifted pulses are injected simultaneously into the lower-transistors of the converter, and two A/D conversion channels are triggered in the pause middles of the dual-pulse for excitation current detection. Two developed sensorless control schemes including the current-rise-time method and current-gradient method are presented based on the decoupled excitation current. The estimated rotor position from the bus current and the actual rotor position from the encoder agree well. Moreover, the BCS position sensorless control is implemented in a speed-controlled system, to show excellent robustness to fast transients.

Compared to other traditional methods, the proposed sensorless system uses only bus current sensor, without the knowledge of motor characteristics and bus voltage. Alternatively, two phase-shifted pulses are injected into the lower-transistors for brief intervals during each current fundamental cycle, which may lead to negligible impact on the phase current or torque. The switching loss is also reduced since only lower-transistors are involved. With this BCS position estimation technique, the sensorless controlled SRM drives will be more robust and compact, which are suited for low-cost and harsh environment applications.

References

[1] K. W. Lee, S. Park, and S. Jeong, "A seamless transition control of sensorless PMSM compressor drives for improving efficiency based on a dual-mode operation," *IEEE Trans. Power Electron.*, vol. 30, no. 3, pp. 1446-1456, Mar. 2015.

[2] Y. Lee, and J. I. Ha, "Hybrid modulation of dual inverter for open-end permanent magnet synchronous motor," *IEEE Trans. Power Electron.*, vol. 30, no. 6, pp. 3286-3299, Jun. 2015.

[3] M. Masoudinejad, S. Feldhorst, F. Javadian, and M. ten Hompel, "Reduction of energy consumption by proper speed selection in PMSM-driven roller conveyors," *IEEE Trans. Ind. Appl.*, vol. 51, no. 2, pp. 1572-1578, Mar./Apr. 2015.

[4] A. V. Sant, V. Khadkikar, X. Weidong, and H. H. Zeineldin, "Four-axis vector-controlled dual-rotor PMSM for plug-in electric vehicles," *IEEE Trans. Ind. Electron.*, vol. 62, no. 5, pp. 3202-3212, May 2015.

[5] H. Chen, and J. J. Gu, "Implementation of the three-phase switched reluctance machine system for motors and generators," *IEEE/ASME Trans. Mechatronics*, vol. 15, no. 3, pp. 421-432, Jun. 2010.

[6] J. Kim, and R. Krishnan, "Novel two-switch-based switched reluctance motor drive for low-cost high-volume applications," *IEEE Trans. Ind. Appl.*, vol. 45, no. 4, pp. 1241-1248, Jul./Aug. 2009.

[7] Y. Kano, T. Kosaka, and N. Matsui, "Optimum design approach for a two-phase switched reluctance compressor drive," *IEEE Trans. Ind. Appl.*, vol. 46, no. 3, pp. 955-964, May/Jun. 2010.

[8] Y. Hu, X. Song, W. Cao, and B. Ji, "New SR drive with integrated charging capacity for plug-in hybrid electric vehicles (PHEVs)," *IEEE Trans. Ind. Electron.*, vol.61, no.10, pp. 5722- 5731, Oct. 2014.

[9] A. Chiba, K. Kiyota, N. Hoshi, M. Takemoto, and S. Ogasawara, "Development of a rare-earth-free SR motor with high torque density for hybrid vehicles," *IEEE Trans. Energy Convers.*, vol. 30, no. 1, pp. 175-182, Mar. 2015.

[10] K. Kiyota, T. Kakishima, and A. Chiba, "Comparison of test result and design stage prediction of switched reluctance motor competitive with 60-kW rare-earth PM motor," *IEEE Trans. Ind. Electron.*, vol. 61, no. 10, pp. 5712-5721, Oct. 2014.

[11] H. C. Chang, and C. M. Liaw, "An integrated driving/charging switched reluctance motor drive using three-phase power module," *IEEE Trans. Ind. Electron.*, vol. 58, no. 5, pp. 1763-1775, May 2011.

[12] J. W. Ahn, S. J. Park, and D. H. Lee, "Novel encoder for switching angle control of SRM," *IEEE Trans. Ind. Electron.*, vol. 53, no. 3, pp. 848-854, Jun. 2006.

[13] M. Ehsani, and B. Fahimi, "Elimination of position sensors in switched reluctance motor drives: state of the art and future trends," *IEEE Trans. Ind. Electron.*, vol. 49, no. 1, pp. 40-47, Feb. 2002.

[14] J. Kim, H. Y. Yang, and R. Krishnan, "Parameter insensitive sensorless control of single-controllable-switch-based switched reluctance motor drive," *IEEE International Conference on Power Electronics and ECCE Asia*, Seoul, Korea, May 2011, pp. 132-139.

[15] B. Fahimi, A. Emadi, and R. B. Sepe, Jr., "Four-quadrant position sensorless control in SRM drives over the entire speed range," *IEEE Trans. Power Electron.*, vol. 20, no. 1, pp. 154-163, Jan. 2005.

[16] G. Gallegos-Lopez, P. C. Kjaer, and T. J. E. Miller, "A new sensorless method for switched reluctance motor drives," *IEEE Trans. Ind. Appl.*, vol. 34, no. 4, pp. 832-840, Jul./Aug. 1998.

[17] C. J. Bateman, B. C. Mecrow, A. C. Clothier, P. P. Acarnley, and N. D. Tuftnell, "Sensorless operation of an ultra-high-speed switched reluctance machine," *IEEE Trans. Ind. Appl.*, vol. 46, no. 6, pp. 2329-2337, Nov./Dec. 2010.

[18] A. Khalil, S. Underwood, I. Husain, H. Klode, B. Lequesne, S. Gopalakrishnan, and A. M. Omekanda, "Four-quadrant pulse injection and sliding-mode-observer-based sensorless operation of a switched reluctance machine over entire speed range including zero speed," *IEEE Trans. Ind. Appl.*, vol. 43, no. 3, pp. 714-723, May/Jun. 2007.

[19] G. Pasquesoone, R. Mikail, and I. Husain, "Position estimation at starting and lower speed in three-phase switched reluctance machines using pulse injection and two thresholds," *IEEE Trans. Ind. Appl.*, vol. 47, no. 4, pp. 1724-1731, Jul./Aug. 2011.

[20] K. W. Hu, Y. Y. Chen, and C. M. Liaw, "A reversible position sensorless controlled switched-reluctance motor drive with adaptive and intuitive commutation tunings," *IEEE Trans. Power Electron.*, vol. 30, no. 7, pp. 3781-3793, Jul. 2015.

[21] E. Ofori, T. Husain, Y. Sozer, and I. Husain, "A pulse-injection-based sensorless position estimation method for a switched reluctance machine over a wide speed range," *IEEE Trans. Ind. Appl.*, vol. 51, no. 5, pp. 3867-3876, Sep./Oct. 2015.

[22] S. Paramasivam, S. Vijayan, M. Vasudevan, R. Arumugam, and R. Krishnan, "Real-time verification of AI based rotor position estimation techniques for a 6/4 pole switched reluctance motor drive," *IEEE Trans. Magn.*, vol. 43, no. 7, pp. 3209-3222, Jul. 2007.
[23] I. H. Al-Bahadly, "Examination of a sensorless rotor-position-measurement method for switched reluctance drive," *IEEE Trans. Ind. Electron.*, vol. 55, no. 1, pp. 288-295, Jan. 2008.
[24] S. A. Hossain, I. Husain, H. Klode, B. Lequesne, A. M. Omekanda, and S. Gopalakrishnan, "Four-quadrant and zero-speed sensorless control of a switched reluctance motor," *IEEE Trans. Ind. Appl.*, vol. 39, no. 5, pp. 1343-1349, Sep./Oct. 2003.
[25] A. Khalil, I. Husain, S. A. Hossain, S. Gopalakrishnan, A. M. Omekanda, B. Lequesne, and H. Klode, "A hybrid sensorless SRM drive with eight- and six-switch converter topologies," *IEEE Trans. Ind. Appl.*, vol. 41, no. 6, pp. 1647-1655, Nov./Dec. 2005.
[26] H. Gao, F. R. Salmasi, and M. Ehsani, "Inductance model-based sensorless control of the switched reluctance motor drive at low speed," *IEEE Trans. Power Electron.*, vol. 19, no. 6, pp. 1568-1573, Nov. 2004.
[27] M. Krishnamurthy, C. S. Edrington, and B. Fahimi, "Prediction of rotor position at standstill and rotating shaft conditions in switched reluctance machines," *IEEE Trans. Power Electron.*, vol. 21, no. 1, pp. 225-233, Jan. 2006.
[28] J. Cai, and Z. Deng, "Sensorless control of switched reluctance motor based on phase inductance vectors," *IEEE Trans. Power Electron.*, vol. 27, no. 7, pp. 3410-3423, Jul. 2012.
[29] Y. T. Chang, K. W. E. Cheng, and S. L. Ho, "Type-V exponential regression for online sensorless position estimation of switched reluctance motor," *IEEE/ASME Trans. Mechatronics*, vol. 20, no. 3, pp. 1351-1359, Jun. 2015.
[30] E. Mese, and D. A. Torrey, "An approach for sensorless position estimation for switched reluctance motors using artifical neural networks," *IEEE Trans. Power Electron.*, vol. 17, no. 1, pp. 66-75, Jan. 2002.
[31] C. A. Hudson, N. S. Lobo, and R. Krishnan, "Sensorless control of single switch-based switched reluctance motor drive using neural network," *IEEE Trans. Ind. Electron.*, vol. 55, no. 1, pp. 321-329, Jan. 2008.
[32] L. Xu, and C. Wang, "Accurate rotor position detection and sensorless control of SRM for super-high speed operation," *IEEE Trans. Power Electron.*, vol. 17, no. 5, pp. 757-763, Sep. 2002.
[33] A. D. Cheok, and Z. Wang, "Fuzzy logic rotor position estimation based switched reluctance motor DSP drive with accuracy enhancement," *IEEE Trans. Power Electron.*, vol. 20, no. 4, pp. 908-921, Jul. 2005.
[34] L. O. de Araujo Porto Henriques, L. G. Barbosa Rolim, W. Issamu Suemitsu, J. A. Dente, and P. J. Costa Branco, "Development and experimental tests of a simple neurofuzzy learning sensorless approach for switched reluctance motors," *IEEE Trans. Power Electron.*, vol. 26, no. 11, pp. 3330-3344, Nov. 2011.
[35] K. R. Thompson, P. P. Acarnley, and C. French, "Rotor position estimation in a switched reluctance drive using recursive least squares," *IEEE Trans. Ind. Electron.*, vol. 47, no. 2, pp. 368-379, Apr. 2000.
[36] K. Ha, R. Y. Kim, and R. Krishnan, "Position estimation in switched reluctance motor drives using the first switching harmonics through fourier series," *IEEE Trans. Ind. Electron.*, vol. 58, no. 12, pp. 5352-5360, Dec. 2011.
[37] J. Cai, and Z. Deng, "Initial rotor position estimation and sensorless control of SRM based on coordinate transformation," *IEEE Trans. Instrum. Meas.*, vol. 64, no. 4, pp. 1004-1018, 2015.
[38] K. R. Geldhof, A. P. M. Van den Bossche, and J. A. Melkebeek, "Rotor-position estimation of switched reluctance motors based on damped voltage resonance," *IEEE Trans. Ind. Electron.*, vol. 57, no. 9, pp. 2954-2960, Sep. 2010.
[39] L. Shen, J. Wu, and S. Yang, "Initial position estimation in SRM using bootstrap circuit without predefined inductance parameters," *IEEE Trans. Power Electron.*, vol. 26, no. 9, pp. 2449-2456, Sep. 2011.
[40] U. Jakobsen, K. Lu, P. O. Rasmussen, D. H. Lee, and J. W. Ahn, "Sensorless control of low-cost single-phase hybrid switched reluctance motor drive," *IEEE Trans. Ind. Appl.*, vol. 51, no. 3, pp. 2381-2387, May/Jun. 2015.
[41] J. Cai, and Z. Deng, "Switched-reluctance position sensor," *IEEE Trans. Magn.*, vol. 50, no. 11, pp. 1-4, Nov. 2014.
[42] J. I. Ha, "Voltage injection method for three-phase current reconstruction in PWM inverters using a single sensor," *IEEE Trans. Power Electron.*, vol. 24, no. 3, pp. 767-775, Mar. 2009.
[43] K. Sung, Q. Wei, L. Huang, and K. Matsuse, "An overmodulation method for PWM-inverter-fed IPMSM drive with single current sensor," *IEEE Trans. Ind. Electron.*, vol. 57, no. 10, pp. 3395-3404, Oct. 2010.
[44] B. Metidji, N. Taib, L. Baghli, T. Rekioua, and S. Bacha, "Low-cost direct torque control algorithm for induction motor without AC phase current sensors," *IEEE Trans. Power Electron.*, vol. 27, no. 9, pp. 4132-4139, Sep. 2012.
[45] B. Metidji, N. Taib, L. Baghli, T. Rekioua, and S. Bacha, "Phase current reconstruction using a single current sensor of three-phase AC motors fed by SVM-controlled direct matrix converters," *IEEE Trans. Ind. Electron.*, vol. 60, no. 12, pp. 5497-5505, Dec. 2013.
[46] H. Shin, and J. I. Ha, "Phase current reconstructions from bus currents in three-phase three-level PWM inverters," *IEEE Trans. Power Electron.,* vol. 29, no. 2, pp. 582-593, Feb. 2014.
[47] C. Gan, J. Wu, S. Yang, and Y. Hu, "Phase current reconstruction of switched reluctance motors from dc-link current under double high-frequency pulses injection," *IEEE Trans. Ind. Electron.*, vol. 62, no. 5, pp. 3265-3276, May 2015.
[48] J. H. Choi, J. S. Ahn, and J. Lee, "The characteristic analysis of switched reluctance motor considering bus voltage ripple on hard and soft chopping modes," *IEEE Trans. Magn.*, vol. 41, no. 10, pp. 4096-4098, Oct. 2005.
[49] H. Kim, M. Falahi, T. M. Jahns, and M. W. Degner, "Inductor current measurement and regulation using a single dc link current sensor for interleaved dc-dc converters," *IEEE Trans. Power Electron.*, vol. 26, no. 5, pp. 1503-1510, May 2011.
[50] K. M. Rahman, and S. E. Schulz, "Design of high-efficiency and high-torque-density switched reluctance motor for vehicle propulsion," *IEEE Trans. Ind. Appl.,* vol. 38, no. 6, pp. 1500-1507, Nov./Dec. 2002.
[51] D. H. Lee, J. Liang, Z. G. Lee, and J. W. Ahn, "A Simple nonlinear logical torque sharing function for low-torque ripple SR drive," *IEEE Trans. Ind. Electron.,* vol. 56, no. 8, pp. 3021-3028, Aug. 2009.
[52] J. Liang, D. H. Lee, G. Xu, and J. W. Ahn, "Analysis of passive boost power converter for three-phase SR drive," *IEEE Trans. Ind. Electron.,* vol. 57, no. 9, pp. 2961-2971, Sep. 2010.
[53] H. Y. Yang, Y. C. Lim, and H. C. Kim, "Acoustic noise/vibration reduction of a single-phase SRM using skewed stator and rotor," *IEEE Trans. Ind. Electron.*, vol. 60, no. 10, pp. 4292-4300, Oct. 2013.

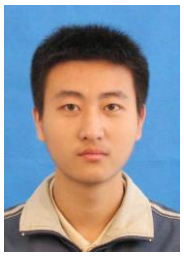

Chun Gan (S'14) received B.S. and M.S. degrees in power electronics and drives from China University of Mining and Technology, Jiangsu, China, in 2009 and 2012, respectively. He is currently working toward Ph.D. degree in the College of Electrical Engineering, Zhejiang University, Hangzhou, China.

His research interests include electrical motor drives, motor design, control with emphasis on switched reluctance motor sensorless technique, and optimization of the torque ripple and efficiency of the motor system.

Jianhua Wu received the B.S. degree from the Nanjing University of Aeronautics and Astronautics, Nanjing, China, and the M.S. and Ph.D. degrees from the Huazhong University of Science and Technology, Huazhong, China, in 1983, 1991, and 1994, respectively, all in electrical engineering.

From 1983 to 1989, he was with Guiyang Electric Company, Guizhou, China, as a Design Engineer. Since 2005, He has been a Professor at the College of Electrical Engineering, Zhejiang University, Zhejiang,

China. He developed the motor design software Visual EMCAD, which is widely used in China. His research interests are electric machine design and drives, including switched reluctance motors, and permanent magnet machines for electric vehicle applications.

Prof. Wu is a Member of the Electrical Steel of Chinese Society for Metals, the Small-Power Machine Committee of China Electrotechnical Society, and the Standardization Administration of China.

Yihua Hu (M'13–SM'15) received the B.S. degree in electrical motor drives and the Ph.D. degree in power electronics and drives from the China University of Mining and Technology, Jiangsu, China, in 2003 and 2011, respectively. Between 2011 and 2013, he was with the College of Electrical Engineering, Zhejiang University, Zhejiang, China, as a Postdoctoral Fellow. Between November 2012 and February 2013, he was an Academic Visiting Scholar with the School of Electrical and Electronic Engineering, Newcastle University, Newcastle, U.K. He is currently a Research Associate with the Department of Electronic and Electrical Engineering, University of Strathclyde, Glasgow, U.K. His research interests include photovoltaic generation system, power electronics converters and control, and electrical motor drives.

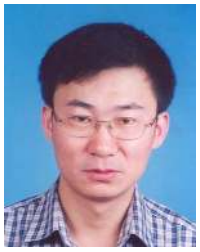

Shiyou Yang received his M.S. degree and Ph.D. degrees from Shenyang University of Technology, Liaoning, China, in 1990 and 1995, respectively, both in electrical engineering.

He is currently a Professor at the College of Electrical Engineering, Zhejiang University, Hangzhou, China. His research interests include computational electromagnetics.

Wenping Cao (M'05–SM'11) received the B.Eng in electrical engineering from Beijing Jiaotong University, Beijing, China, in 1991, and the Ph.D. degree in electrical machines and drives from the University of Nottingham, Nottingham, U.K., in 2004.

He is currently a Marie Curie Fellow with the Department of Electrical Engineering and Computer Science, Massachusetts Institute of Technology, Cambridge, MA, USA, and a Chair Professor of Electrical Power Engineering with Aston University, Birmingham, U.K. His research interests include fault analysis and condition monitoring of electric machines and power electronics.

Prof. Cao was the recipient of the Best Paper Award at the 2013 International Symposium on Linear Drives for Industry Applications (LDIA), the Innovator of the Year Award from Newcastle University, Newcastle upon Tyne, U.K., in 2013, and the Dragon's Den Competition Award from Queen's University Belfast in 2014. He serves as an Associate Editor for IEEE TRANSACTIONS ON INDUSTRY APPLICATIONS, *IEEE Industry Applications Magazine* and *IET Power Electronics*. He is also the Chief Editor for three Special Issues and one book, and an Editor for *Electric Power Components and Systems* Journal as well as nine other International Journals. Prof. Cao is also a Member of the Institution of Engineering and Technology and a Fellow of Higher Education Academy.

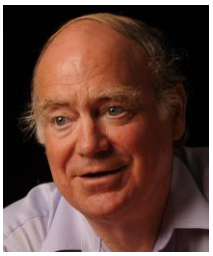

James L. Kirtley, Jr. (LF'91) received the Ph.D. degree from the Massachusetts Institute of Technology (MIT), Cambridge, MA, USA, in 1971.

He is a Professor of electrical engineering with the Department of Electrical Engineering and Computer Science, School of Engineering, MIT. His research interests include electric machinery and electric power systems.

Prof. Kirtley served as the Editor-in-Chief of the IEEE TRANSACTIONS ON ENERGY CONVERSION from 1998 to 2006 and continues to serve as an Editor for the journal, and he is a member of the Editorial Board of Electric Power Components and Systems. He was the recipient of the IEEE Third Millennium Medal in 2000 and the Nikola Tesla Prize in 2002. He was elected to the U.S. National Academy of Engineering in 2007.